Additive Manufacturing 102 (2025) 104720

Contents lists available at ScienceDirect

Additive Manufacturing

journal homepage: www.elsevier.com/locate/addma

Low Young's modulus in laser powder bed fusion processed Ti–15Mo–5Zr–3Al alloys achieved by the control of crystallographic texture combined with the retention of low-stability bcc structure

Shota Higashino [a], Daisuke Miyashita [a], Takuya Ishimoto [b,c,d], Eisuke Miyoshi [a], Takayoshi Nakano [b,c], Masakazu Tane [a,b,c,*]

[a] Graduate School of Engineering, Osaka Metropolitan University, 1-1 Gakuen-cho, Nakaku, Sakai, Osaka 599-8531, Japan
[b] Division of Materials and Manufacturing Science, Graduate School of Engineering, The University of Osaka, 2-1 Yamadaoka, Suita, Osaka 565-0871, Japan
[c] Anisotropic Design and Additive Manufacturing Research Center, The University of Osaka, 2-1 Yamadaoka, Suita, Osaka 565-0871, Japan
[d] Aluminium Research Center, University of Toyama, 3190 Gofuku, Toyama, Toyama 930-8555, Japan

ARTICLE INFO

Keywords:
Laser powder bed fusion
Elastic properties
Titanium alloys
Crystallographic texture
ω phase transformation

ABSTRACT

Metastable β (body-centered cubic)-phase Ti alloys, quenched from a high-temperature β-phase field, have attracted great interest as biomedical implants, owing to their low Young's modulus. Recently, the application of additive manufacturing (AM) to β-phase Ti alloys has gathered much attention, because the AM process can form anisotropic crystallographic texture in which an elastically soft direction is preferentially oriented, resulting in low Young's modulus in a specific direction. However, the effects of anisotropic texture and microstructure formed by the AM process on anisotropic elastic properties have not been clarified in detail. In the present study, we measured all the independent elastic stiffness components of β-phase Ti–15Mo–5Zr–3Al (mass%) alloys, prepared by bidirectional scanning with (XY-scan) and without (X-scan) an interlayer rotation of 90° in laser powder bed fusion (LPBF), one of the AM processes, using resonant ultrasound spectroscopy. The measurements revealed that the LPBF-processed Ti alloys exhibited strong elastic anisotropy and a low Young's modulus (below 60 GPa) in the <100>-oriented direction of the alloy prepared by the XY-scan. Furthermore, micromechanics calculations based on Eshelby's inclusion theory revealed that the single crystal constituting the alloys prepared by LPBF had almost the same elastic stiffness as that of a single crystal prepared by the floating zone melting, which indicated that the metastable β phase was retained by suppressing an easily occurring β- to ω-phase transformation during LPBF. These results indicate that texture control combined with retention of the metastable β phase by LPBF achieves biocompatible low Young's modulus.

1. Introduction

Ti and its alloys are widely used to fabricate biomedical implants such as artificial hip joints, bone fixation plates, and dental implants [1] owing to their biocompatibility and high mechanical strength. In addition, recent studies have underscored the necessity of reducing Young's modulus of Ti alloys developed for medical implant applications. This reduction aims to prevent stress shielding, a phenomenon that can degrade bone tissue [2].

In metastable β-phase Ti alloys with a low stability body-centered cubic (bcc) crystal structure, Young's modulus is low compared to other Ti alloy crystal structures [2]. Therefore, metastable β-phase Ti alloys are promising candidates for fabricating biomedical implants [2,3]. However, in most isotropic polycrystalline β-phase Ti alloys, Young's modulus is much higher than that of human bones. To overcome this problem, the formation of an anisotropic crystallographic texture in which an elastically soft <100> direction is preferentially oriented in a specific direction can be utilized. However, achieving this preferential orientation using conventional cold- or hot-working processes is difficult.

Recently, additive manufacturing (AM) has gained considerable attention owing to its design flexibility, which is enabled by manipulating a highly localized heat source, such as a laser or an electron beam [4]. Importantly, the AM process can control the crystallographic

---

[*] Corresponding author at: Graduate School of Engineering, Osaka Metropolitan University, 1-1 Gakuen-cho, Nakaku, Sakai, Osaka 599-8531, Japan.
E-mail address: tane@mat.eng.osaka-u.ac.jp (M. Tane).

https://doi.org/10.1016/j.addma.2025.104720
Received 15 November 2024; Received in revised form 20 February 2025; Accepted 22 February 2025

texture through localized melting and rapid cooling, and by manipulating the scanning parameters of the heat source [4–7]. In a previous study [8], laser powder bed fusion (LPBF) was used to control the crystallographic texture of a metastable Ti–15Mo–5Zr–3Al (mass%) alloy, referred to as Ti-1553. However, the effect of the anisotropic crystallographic texture on the anisotropic elastic properties has not been investigated in detail.

In addition to the formation of crystallographic texture, retention of a single β-phase state is important to obtain a low Young's modulus in metastable β-Ti alloys prepared by AM. In metastable β-Ti alloys, a phase transformation from metastable β- to ω (hexagonal)-phase easily occurs by annealing at ~525–650 K, quenching, deformation, and even by aging at near room temperature [9–14]. The elastic modulus of the ω phase is higher than that of the β phase, and thus, ω-phase formation increases Young's modulus [15]. Therefore, suppressing ω-phase formation is essential to achieve a low Young's modulus. In β-Ti alloys prepared by AM, the ω-phase possibly forms from heat accumulation during the building process [16–20]. Notably, a large build size forms an extensive nanoscale ω-phase, raising the difficulty in achieving a low Young's modulus in more practical large-sized products [19]. In a previous study of alloy Ti-1553, electron beam powder bed fusion (EBPBF) process was employed to prepare the alloy products, which resulted in the formation of a small amount of ω phase due to the preheating process for each building layer [21]. Therefore, the single β-phase state cannot be retained by EBPBF. Another important AM process, LPBF, possibly shows promise for increasing the retention of single β-phase microstructure in Ti alloys. However, the effect of LPBF on ω-phase formation in β-phase Ti alloys and its correlation with elastic properties have not yet been revealed.

In the present study, we investigated the anisotropic elastic properties of β-phase Ti-1553 alloy prepared by the two-types of laser scanning strategies in the LPBF process, focusing on the effects of crystallographic texture and ω-phase formation on elastic properties. To develop a comprehensive understanding of anisotropic elastic properties, a complete set of the independent elastic stiffness components of LPBF-processed anisotropic alloys was measured using resonant ultrasound spectroscopy integrated with laser Doppler interferometry (RUS-LDI). The RUS-LDI measurements revealed anisotropic elastic properties that reflect the scan-dependent crystallographic texture, and that the lowest Young's modulus ($<$ 60 GPa) was obtained along the direction which showed the strongest <100> orientation. Furthermore, the effects of crystallographic texture and ω-phase formation on anisotropic elastic properties were analyzed by micromechanics models based on Eshelby's inclusion theory, Mori-Tanaka mean-field theory, and effective-medium approximation. The analyses indicated the importance of not only texture control but also the retention of the single, metastable β-phase in reducing Young's modulus of the alloys prepared by the AM process.

2. Material and methods

2.1. Preparation of XY- and X-scan products with controlled crystallographic texture

Ti-1553 alloy products with controlled crystallographic textures were prepared using LPBF [8]. An ingot with a nominal composition of Ti-1553 was atomized to spherical powders (Fig. 1a) [22] through Ar gas-atomization (Osaka Titanium Technologies, Japan). The particle size distribution (Fig. 1b) was measured using a Mastersizer 3000E particle size analyzer (Malvern Panalytical, UK) with D10 = 19.0 μm, D50 = 31.6 μm, and D90 = 50.3 μm. Samples with the dimensions of 5 mm (depth) × 5 mm (length) × 10 mm (height) were prepared using a LPBF apparatus (EOS M 290, EOS, Germany). A Yb fiber laser was used at the laser power, scanning speed, scan pitch, and layer thickness of 360 W, 1200 mm/s, 100 μm, and 60 μm, respectively. The LPBF was performed in an Ar gas atmosphere.

Two scan strategies [8] were employed in this study to prepare the LPBF products with different crystallographic textures (Figs. 2a-1 and 2b-1). The X, Y, and Z axes represent the coordinates of the sample coordinate system. One of the scan strategies employed is bidirectional scanning, wherein the material is repeatedly scanned along the X- and Y-axes with an interlayer rotation of 90° (Fig. 2a-1). This scan is referred to as an XY-scan. The other scan strategy is bidirectional scanning along the X-axis (Fig. 2b-1). This scan is referred to as an X-scan.

From the prepared products, cubic samples of approximately $4 \times 4 \times 4$ mm^3 were cut via electrical discharge machining and polished using emery paper up to 2000 grit for subsequent characterization of elastic properties.

2.2. Microstructure characterizations

Microstructures and elemental distributions were investigated using field-emission scanning electron microscopy (FE-SEM; JIB-4610F, JEOL, Japan) and energy-dispersive X-ray spectroscopy (EDS; Aztec 3.1, Oxford Instruments, UK) mounted on the FE-SEM. EDS was operated at an acceleration voltage of 20 kV. To obtain information on crystal orientation distribution, inverse pole figure (IPF) images were obtained using an electron backscatter diffraction (EBSD) system (NordlysMax^3; Oxford Instruments, UK) equipped with the FE-SEM. EBSD was operated at an acceleration voltage of 20 kV and a step size of 3 μm. For EDS and EBSD analysis, the specimen surfaces were polished with emery papers and subsequently mirror polished with colloidal silica.

EBSD detects only the crystallographic texture of the specimen surface. To address this limitation, EBSD analyses were performed on all the specimens used for the measurement of elastic properties: four samples for XY-scan products and four samples for X-scan products. Furthermore,

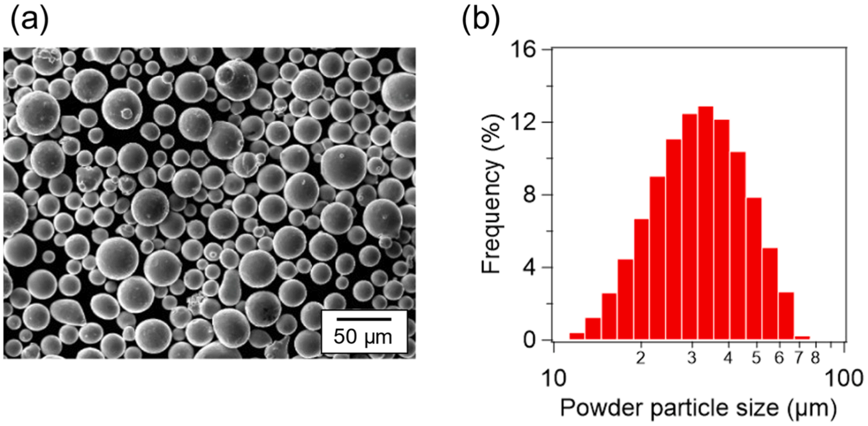

Fig. 1. (a) SEM image of the Ti-1553 pre-alloyed powder used for LPBF and (b) the frequency distribution of the particle size of powders. Panel (a) is reproduced from the literature [22], published under the CC BY 4.0 license.

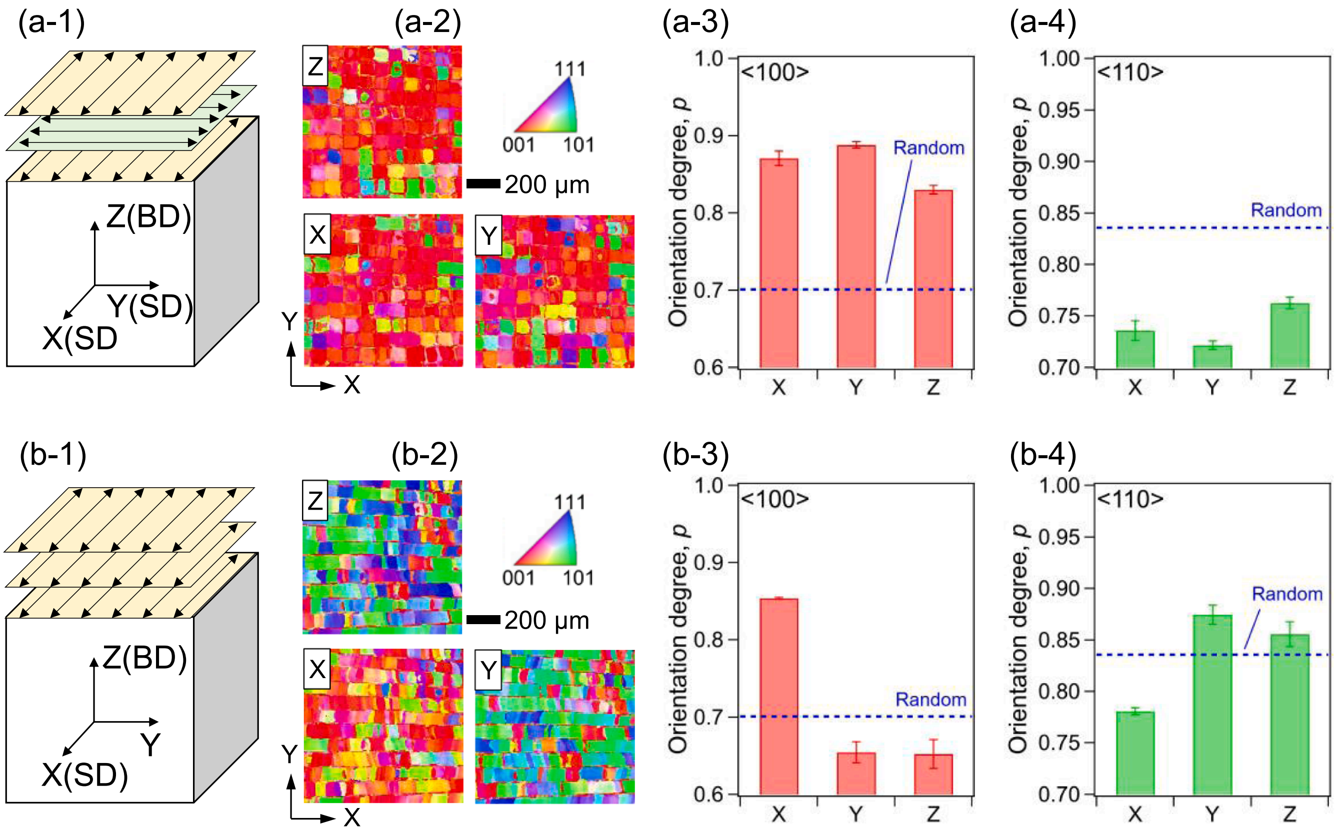

Fig. 2. Schematic for (a-1) XY- and (b-1) X-scans in the LPBF process. IPF maps of the (a-2) XY- and (b-2) X-scan products obtained from the XY plane and projected along the X-, Y-, and Z-axes. Orientation degrees *p* for the <100> directions along the X-, Y-, and Z-axes of the (a-3) XY- and (b-3) X-scan products and those for the <110> directions of the (a-4) XY- and (b-4) X-scan products.

the analyses were conducted over a wide area of 2.853 × 2.853 mm^2 for each specimen.

A transmission electron microscope (TEM; JEM-3010, JEOL, Japan) operating at 300 kV was used for phase analysis. The foil samples for TEM observations were thinned using a twin-jet machine (Tenupol-3, Struers, Denmark) with a solution comprising 5 % $HClO_4$, 30 % butanol, and 65 % methanol at approximately 263 K.

2.3. *Elastic properties*

As described below in the Experimental results section, the LPBF-processed XY- and X-scan products obtained in this study were expected to exhibit different Young's moduli along the X-, Y-, and Z-axes owing to their crystallographic texture. Therefore, the elastic stiffness components of the XY- and X-scan products were measured via RUS [23] integrated with LDI [24] (RUS-LDI) at approximately 298 K. The products possessed orthorhombic elastic symmetry, as described in Section 3.4. in Supplementary Materials. Supplementary Fig. S1 shows the experimental setup for RUS-LDI. A detailed analysis of the elastic properties and corresponding explanations are provided in the Supplementary Materials. In the RUS analysis, the vibration frequency was swept from 100 kHz to 1 MHz to determine the resonance frequency of the sample. The obtained resonance frequencies were used for the LDI analysis to determine the vibration mode for each frequency.

The directional dependence of the Young's moduli of the XY- and X-scan products was examined using the elastic stiffness components obtained by RUS-LDI. Mathematica version 12 (Wolfram Research, Inc.) and AnisoVis software written in MATLAB were used for the calculation and three-dimensional (3D) visualization of Young's moduli [25].

3. Experimental results

3.1. *Crystallographic texture and elemental segregation formed in XY- and X-scan products*

Ti-1553 alloy products were prepared using the XY- and X-scan strategies. Fig. 2a-2 shows the IPF maps obtained through scanning electron microscope/EBSD analysis in the XY plane of the XY-scan products, where the XY plane is perpendicular to the Z-axis. IPF maps in planes perpendicular to the X- and Y-axes were obtained by projecting the crystallographic orientation observed along the Z-axis onto the X- and Y-axes, respectively. Therefore, the IPF map in the plane perpendicular to the Z-axis represents both the actual grain shape and crystallographic orientation, whereas those in the planes perpendicular to the X- and Y-axes represent only the crystallographic orientation and not the grain shape.

As shown in the IPF maps (Fig. 2a-2), the <100> directions were oriented along the X-, Y-, and Z-axes under the XY-scan. However, in the X-scan (Fig. 2b-2), the <100> directions were oriented along the X-axis, whereas the <110> directions were oriented along the Y- and Z-axes. The formation mechanism of the <100> and <110> orientations under the two scan strategies was elucidated in a previous study [8,26]. In brief, <100> growth in the directions inclined ± 45° to building direction (BD) in the melt pool cross-section in the X-scan, and that in the directions 0° and 90° from BD in the XY-scan, resulted in the formation of the above-described crystallographic orientations. The stabilized orientation is geometrically determined by the self-adjustment of crystallographic orientation driven by the reduction of crystallographic misorientation at the fusion boundary where the two solid-liquid interfaces encounter in melt pool, and by the availability of epitaxial growth from adjacent and underlying melt pools. Such stabilization of crystallographic orientation is governed by the melt pool shape [27].

The crystallographic textures of the prepared products were quantitatively analyzed using the orientation degree, p, which is defined as follows [28]:

$$p = \frac{1}{N}\sum_{i=1}^{N}\cos^2\gamma_i, \tag{1}$$

where N is the number of EBSD data points, each of which provides a set of Euler angles, and γ_i is the angle between the coordinate axes of the sample coordinate system (X-, Y-, and Z-axes) and either the <100> or <110> direction. As a cubic crystal has 6 and 12 equivalent crystallographic <100> and <110> directions, respectively, the smallest angle between the sample coordinate axes and one of the equivalent crystallographic directions was defined as γ_i. According to this definition, a high value of p indicates a high degree of crystallographic orientation, with the maximum value of p being 1.

Fig. 2a-3 shows the orientation degree p for the <100> orientation along the X-, Y-, and Z-axes of the XY-scan products. For comparison, the p-value for a random polycrystal (0.7008) is also shown [28]. The average values and standard deviations of p for the XY-scan products were obtained for all four samples. The standard deviations of p are negligible, indicating that the four prepared products have similar crystallographic textures. As shown in Fig. 2a-3, the p values for the <100> orientation were clearly higher than those of the random polycrystal, indicating that the XY-scan products exhibited a high degree of <100> orientation along the X-, Y-, and Z-axes. The strongest <100> orientation was observed along the Y-axis, followed by the X-axis, while the weakest orientation was formed along the Z-axis. The stronger <100> orientation along the X- and Y-axes compared to the Z-axis can be attributed to the preferential stabilization of the <100> orientation during scanning along the X- and Y-directions [28]. Reflecting the high degree of the <100> orientation in the XY-scan products, the p values for the <110> orientation were low compared to those of the random polycrystal (0.8354) (Fig. 2a-4), where the orientation degree for the random polycrystal is shown as “Random” with a dotted line [28]. By contrast, the X-scan products exhibited a predominant <100> orientation along the X-axis (Fig. 2b-3), whereas the <110> directions were oriented along the Y- and Z-axes (Fig. 2b-4). Notably, the <110> orientation was stronger along the Y-axis than along the Z-axis (Fig. 2b-4).

Fig. 3 shows (a) the backscattered electron (BSE) image observed in the YZ plane of the X-scan products, along with the EDS mappings of (b) Ti, (c) Mo, (d) Zr, and (e) Al elements analyzed in the area shown in (a). The BSE image indicated the presence of small elemental segregation, but distinct elemental segregation was not detected in the EDS mappings of any of the elements. Fig. 3f shows the concentrations of Ti, Mo, Zr, and Al elements along the line in Fig. 3a, obtained through EDS analysis. The line profiles indicate that the elemental distribution is almost homogeneous. This homogeneity in the elemental distribution is probably attributed to the small solidification interval that is the difference between the solidus and liquidus temperatures. In the Ti-1553 alloy, the evaluation using the JMatPro software indicated that the solidification interval is as small as 20 K [22]. In addition to this small solidification interval, the rapid quenching rate of approximately 10^6 K/s during LPBF suppresses constitutional undercooling. As a result of both the small solidification interval and the rapid quenching rate, the elemental distribution in the LPBF-processed Ti-1553 alloy was homogeneous.

3.2. Shape of grains in XY- and X-scan products

Fig. 4 shows the IPF maps of the (a) XY- and (b) X-scan products obtained from the YZ plane. Both the products prepared under the X- and XY-scans exhibited column-shaped grains elongated along the building direction (Z). This formation of columnar grains was attributed to epitaxial grain growth across multiple melt pools from previously solidified parts [8].

To quantitatively evaluate the grain shape, high-angle grain

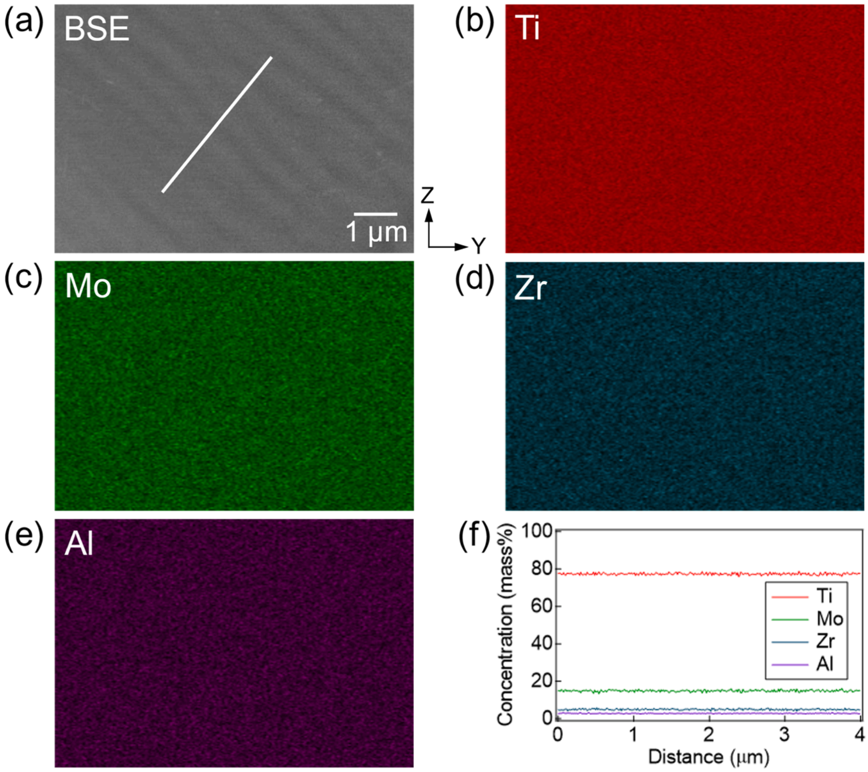

Fig. 3. (a) BSE image observed in the YZ plane of the X-scan products, and EDS mappings of (b) Ti, (c) Mo, (d) Zr, and (e) Al elements analyzed in the area shown in (a). (f) Concentrations of Ti, Mo, Zr, and Al elements along the line in (a), obtained through EDS analysis.

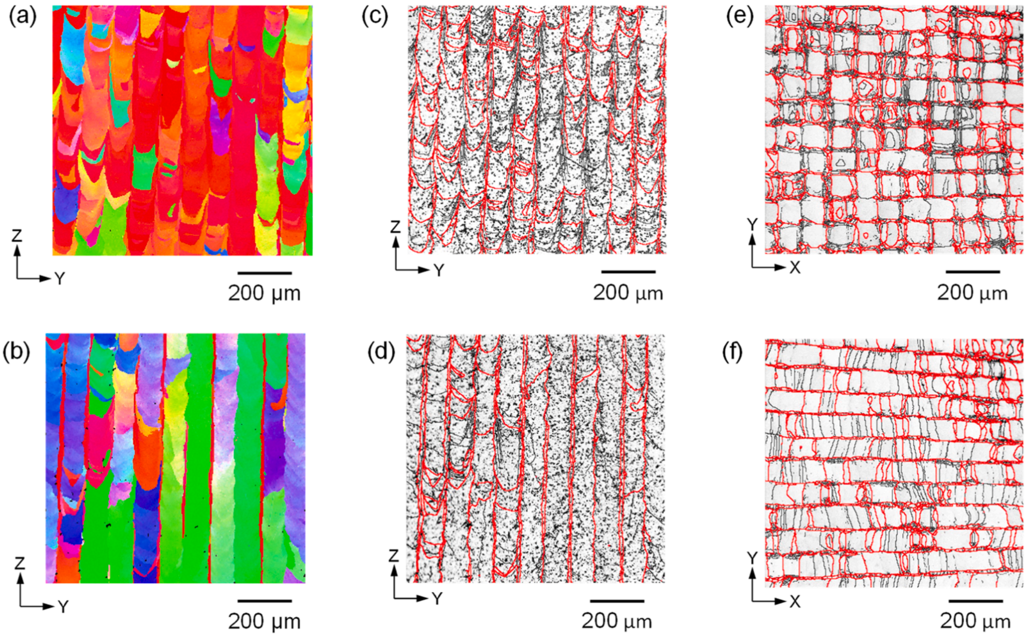

Fig. 4. IPF maps of (a) XY- and (b) X-scan products obtained from the YZ-plane. EBSD grain boundary maps for the YZ planes of the (c) XY- and (d) X-scan products and those for the XY planes of (e) XY- and (f) X-scan products. High-angle grain boundaries are shown as red lines and low-angle grain boundaries as black lines.

boundaries with a crystallographic misorientation angle exceeding 15° and low-angle grain boundaries with a tilt angle between 2° and 15° were analyzed using the IPF maps. Fig. 4 shows EBSD grain boundary maps, where high-angle grain boundaries are shown as red lines and low-angle grain boundaries as black lines, for the YZ planes of the (c) XY- and (d) X-scan products. To analyze the aspect ratio of the grains

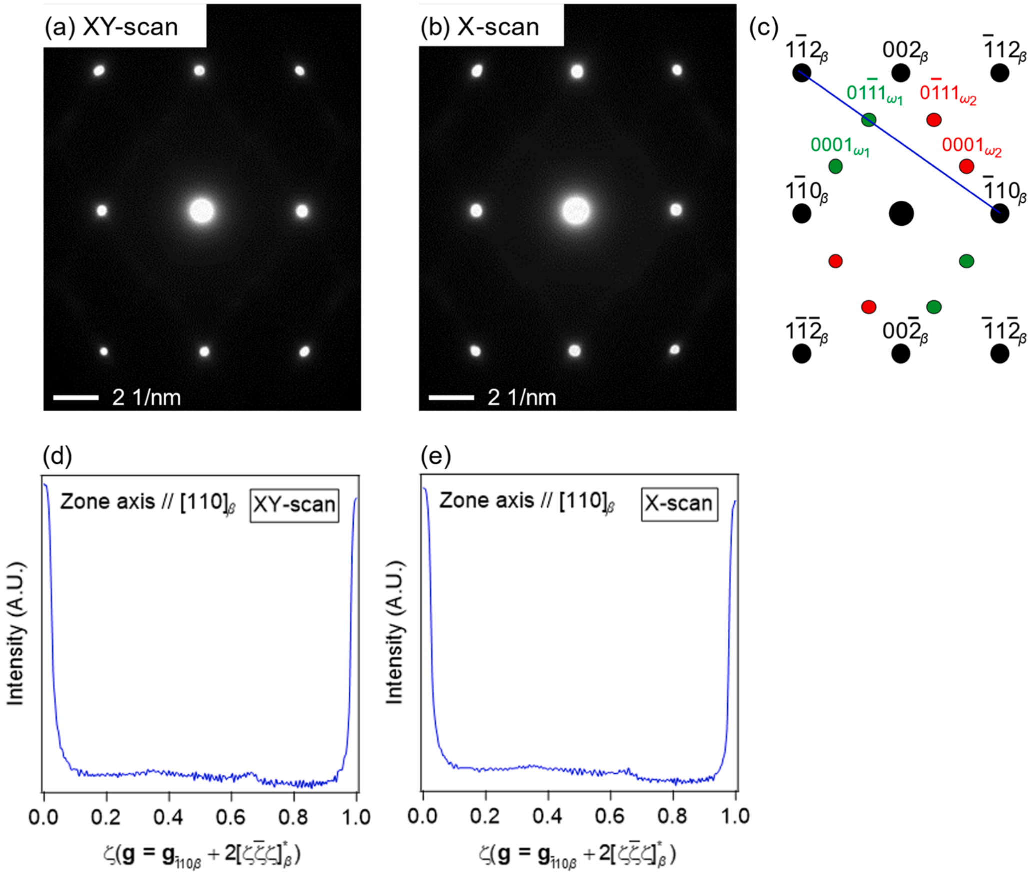

Fig. 5. Electron diffraction patterns of the (a) XY-scan and (b) X-scan products obtained along the $[110]_\beta$ direction. (c) Key diagram of the electron diffraction spots derived from the β-phase (black) and two domains of ω phases (green and red). One dimensional intensity profile along the $[\zeta\bar{\zeta}\zeta]^*_\beta$ direction of electron diffraction patterns of (d) XY-scan and (e) X-scan products.

observed in the YZ planes, the grain boundary was defined as a high-angle grain boundary in which the tilt angle of the crystallographic misorientation exceeded 15°. The aspect ratio of the grains in the YZ plane is defined as the ratio of the length along the Z-axis to that along the Y-axis. In addition, to eliminate noise pixels that erroneously contribute to the appearance of small-sized grains, a grain size of 10000 μm^2 was employed as a threshold [29], aligning with the typical grain size observed in Ti-1553 alloys prepared via LPBF [8]. With this definition of grain boundary, the average aspect ratios of grains in the XY- and X-scan products were calculated as 3.2 and 7.4, respectively. The error introduced in the aspect ratios upon changing the threshold between 0 and 10000 μm^2 was less than 7 % for both products.

In Fig. 4, the EBSD grain boundary maps for the XY planes of the (e) XY- and (f) X-scan products are also shown. In the XY planes, the aspect ratio of the grains, defined as the ratio of the length along the X-axis to that along the Y-axis, was evaluated. The evaluation indicated that the aspect ratios of grains in the XY- and X-scan products were 2.4, suggesting that the grains were slightly elongated along the X-axis.

3.3. Phase constitution of XY- and X-scan products

Fig. 5a shows the electron diffraction pattern of the XY-scan product obtained along the $[110]_\beta$ direction. Compared to the key diagram of the electron diffraction spots (Fig. 5c), the obtained diffraction pattern in Fig. 5a is attributed solely to a bcc-structured β phase [30]. Moreover, the X-scan products were composed of β-phase (Fig. 5b).

Fig. 5 shows the one-dimensional intensity profile along the $[\zeta\bar{\zeta}\zeta]^*_\beta$ direction of the electron diffraction patterns of the (d) XY-scan and (e)X-scan products. Small broad peaks appeared at $\zeta \cong 2/3$, indicating that a tiny fraction of the ω phase was formed. Notably, similar broad peaks at $\zeta \cong 1/3$ appeared owing to the double diffraction. In metastable β-phase Ti alloys with low β-phase stability, a similarly small fraction of the ω phase is formed [31,32]. This formation of the ω phase occurs in locally unstable β-phase regions, which are created by quenched-in statistical compositional fluctuations that inevitably exist even when constituent elements are randomly distributed [14]. Therefore, it is deduced that the formation of the ω phase was suppressed in the XY-scan and X-scan products. This suppression of the ω phase could be attributed both to the Al addition [31] and to the rapid quenching rate of approximately 10^6 K/s during LPBF, which hinders isothermal ω transformation [33].

3.4. Elastic stiffness components of XY- and X-scan products

The elastic stiffness components (c_{ij}) of the XY- and X-scan products were measured by RUS-LDI. As described in Section 3.1, the XY-scan products exhibited a <100>-oriented texture along all three coordinate (X, Y, and Z) axes, whereas the X-scan products exhibited <100>-oriented texture along the X-axis and <110>-oriented texture along the Y- and Z-axes. These textures in the XY- and X-scan products approximately results in macroscopic cubic and tetragonal elastic symmetries, respectively. However, to detect detailed differences in the orientation degree among the axes, as can be encountered in LPBF products, the elastic properties were analyzed under the assumption of an orthorhombic elastic symmetry with nine independent elastic stiffness components. Section 3.4 in the Supplementary Materials validates this assumption through the numerical estimation of the elastic stiffness of XY- and X-scan products using a micromechanics model called self-consistent (SC) approximation [34–36], which is based on Eshelby's inclusion theory [37] and effective-medium approximation [38]. The measured c_{ij} components with nine independent components were referenced to the reference coordinates ($x_1x_2x_3$), which are the same as the sample coordinates (XYZ) (Figs. 6a and 6b). The Young's modulus in the x_1 reference axis (E_1) of the sample was calculated using the elastic compliance component s_{11}:

$$E_1 = 1/s_{11}. \tag{2}$$

Similarly, E_2 and E_3, which are Young's moduli along the x_2- and x_3-axes, respectively, were calculated using the elastic compliance components s_{22} and s_{33}.

Table 1 lists the c_{ij}, E_1, E_2, and E_3 values of the XY- and X-scan products with an orthorhombic elastic symmetry. The averages and standard deviations were obtained from four samples. Notably, each c_{ij} component exhibited only a small standard deviation, typically less than 5 %, indicating that the obtained elastic stiffness is statistically reliable. For the XY-scan products, the c_{11} and c_{22} components differed slightly, although the products exhibited an <100> orientation along both the x_1- and x_2-axes. Furthermore, for the X-scan product, the c_{22} and c_{33} components were different, although this product had similar <110> orientations along both the x_2- and x_3-axes. The differences between the c_{11}, c_{22}, and c_{33} components of the XY- and X-scan products indicate that both products have orthorhombic elastic symmetry, reflecting their anisotropic crystallographic textures and grain shapes.

3.5. Directional dependence of Young's modulus in XY- and X-scan products

Visualizing the directional dependence of Young's moduli of XY- and X-scan products in 3D space aids in understanding their elastic anisotropy. Fig. 6a shows a schematic of the preferential orientation of the XY-scan product and the corresponding 3D plot of Young's modulus, where SD and BD denote scanning and building directions, respectively. The

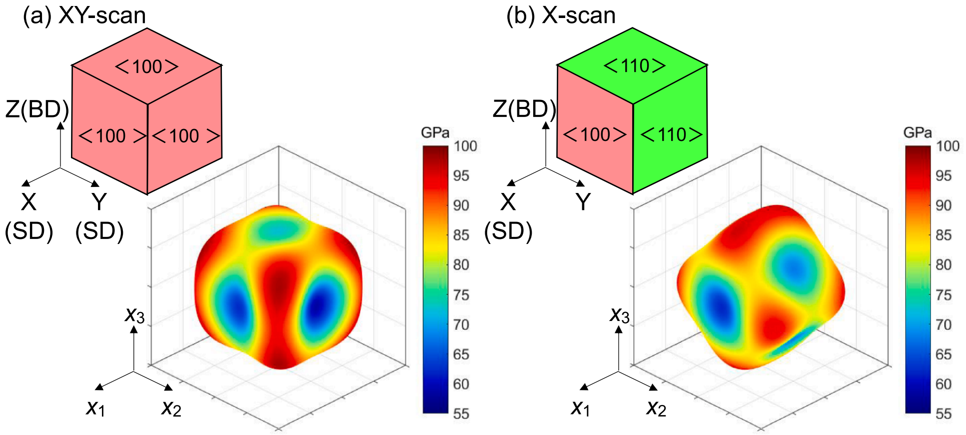

Fig. 6. Schematic of the crystallographic orientation and 3D plots of Young's modulus for the (a) XY- and (b) X-scan products. The X-, Y-, and Z-axes of these two products were aligned referring to the Cartesian coordinate system (x_1, x_2, x_3) shown on the left of the 3D plots.

Table 1

Elastic stiffness components c_{ij} (GPa) and Young's modulus in x_1, x_2, and x_3 directions, E_1, E_2, and E_3 (GPa), of the XY- and X-scan products with orthorhombic elastic symmetry. The values were measured using the RUS-LDI method. The mean and standard deviations of c_{ij} and E_i were obtained from four samples.

	c_{11}	c_{22}	c_{33}	c_{23}	c_{13}	c_{12}
XY-scan	145.1 ± 4.4	140.4 ± 2.8	152.8 ± 5.3	99.2 ± 1.5	99.0 ± 2.0	101.8 ± 2.3
X-scan	139.2 ± 1.2	162.7 ± 7.9	177.9 ± 6.3	101.0 ± 3.0	102.7 ± 1.9	101.8 ± 3.3
	c_{44}	c_{55}	c_{66}	E_1	E_2	E_3
XY-scan	35.5 ± 0.4	33.4 ± 0.8	39.1 ± 0.4	62.3 ± 1.6	58.5 ± 1.2	72.3 ± 2.0
X-scan	23.8 ± 0.4	33.1 ± 0.8	35.1 ± 0.2	62.0 ± 0.8	81.6 ± 2.8	94.4 ± 3.1

3D plots were obtained using AnisoVis software [25] through coordinate conversion of the measured c_{ij} (Table 1). In the 3D plot, the radius in any direction from the origin to the surface is proportional to the magnitude of Young's modulus in that direction. Young's modulus is also represented by a color map of the 3D surface.

In the XY-scan product (Fig. 6a), Young's moduli along the X- and Y-axes were notably lower than those along the Z-axis, even though the XY-scan product exhibited an <100> orientation along all the X-, Y-, and Z-axes. As shown in Fig. 6b, in the X-scan product, Young's moduli along the Y- and Z-axes, along which the <110> orientation was observed, were higher than those along the X-axis. Note that the Young's modulus along the Y-axis was notably lower than that along the Z-axis. These results indicate that in both the XY- and X-scan products, Young's moduli in the scanning directions (the X- and Y-axes for the XY-scan and the X-axis for the X-scan) were low, originating from the <100> orientation.

For the XY-scan product, relatively low Young's moduli were obtained in E_1 for the SD of the X-axis and in E_2 for the SD of the Y-axis, as shown in Table 1. This value was attributed to the high degree of crystallographic orientation along these axes (Fig. 2a-3). The lowest Young's modulus achieved in E_2 for the Y-axis SD of the XY-scan product was 58.5 ± 1.2 GPa, which is close to that of human bone [31]. These results indicate that the XY scan was more favorable for achieving a low Young's modulus.

The relationship between the elastic anisotropies of the XY- and X-scan products was examined through coordinate conversion around the x_1 axis (Supplementary Fig. S2). When the XYZ coordinate system was rotated by 45° along the x_1-axis of the reference $x_1x_2x_3$ coordinate system, the directional dependence of Young's modulus in the XY-scan product was almost the same as that in the X-scan product. This indicates that a similar crystallographic texture was formed in the XY- and X-scan products; however, the XY-scan products exhibited a lower Young's modulus owing to the high degree of <100> orientation.

3.6. *Comparison of Young's moduli in XY- and X-scan products with those in single crystal and random polycrystal*

Fig. 7a shows the directional dependence of Young's modulus of an XY-scan product in relation to the angle θ (0–90°). Here, θ is defined as an angle from the x_2- to the x'-axis, which makes an angle of 90° from the x_2-axis and 45° from the x_1- and x_3-axes. With this definition of θ, an increase of θ expresses a directional change from <100> to <111>, followed by a transition to the <110> direction. For comparison, the directional dependence of Young's modulus in a Ti-1553 single crystal [31] and its random polycrystal are also shown. To calculate Young's modulus of the Ti-1553 single crystal, the cubic lattice vectors were assumed to be parallel to the reference coordinates. The Young's modulus of a random polycrystal, E_{RP}, for a cubic crystal structure, was calculated by the Voigt-Reuss-Hill (VRH) approximation [31,39] as follows:

$$E_{\mathrm{RP}} = \frac{1}{2}(E_{\mathrm{V}} + E_{\mathrm{R}})$$

$$= \frac{1}{2}\left(\frac{9}{\dfrac{1}{B} + \dfrac{15}{2c' + 3c_{44}}} + \frac{5}{\dfrac{5}{9B} + \dfrac{2}{3c'} + \dfrac{1}{c_{44}}}\right), \qquad (3)$$

where E_{RP} is obtained as the arithmetic mean of E_{V} and E_{R}, which are the Young's moduli of the polycrystals calculated using the Voigt and Reuss approximations, respectively. B is the bulk modulus and $c' = (c_{11} - c_{12})/2$ is the shear modulus for the $\{110\}\langle 1\bar{1}0\rangle$ shear, respectively. The VRH approximation is not necessarily the arithmetic mean of the Voigt and Reuss bounds, as expressed in Eq. (3), but can also be a geometric mean [40]. However, in this study, the arithmetic mean in Eq. (3) was employed, because it is known to be close to experimental values [40, 41].

As shown in Fig. 7a, Young's modulus of the XY-scan product exhibited weaker anisotropy than that of the single crystal. However, the

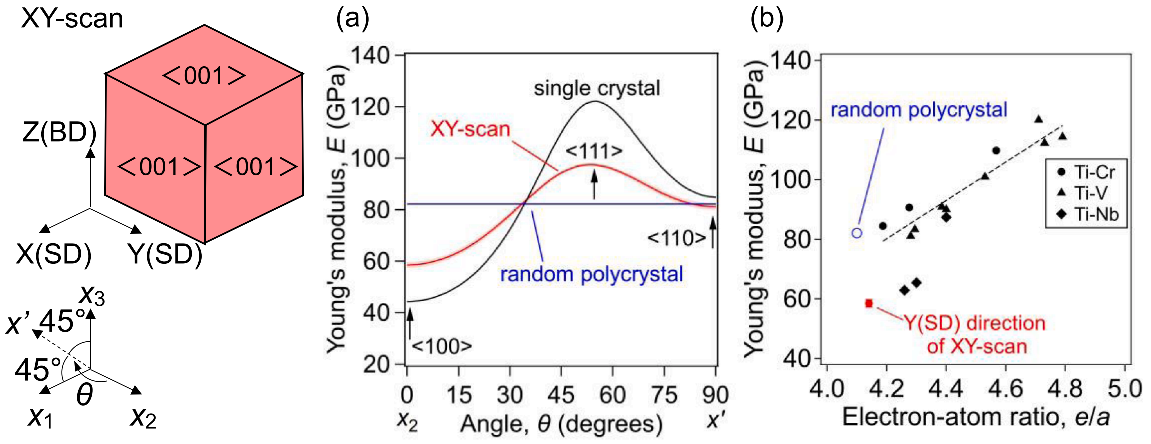

Fig. 7. (a) Directional dependence of Young's modulus of the XY-scan products calculated from the measured elastic stiffness components c_{ij}. Directional dependence of Young's modulus of a single crystal [31] and a random polycrystal are also compared. (b) Comparison between Young's modulus in the Y direction (E_2) of the XY-scan products and that of random polycrystal E_{RP} of alloy Ti-1553 with respect to the e/a ratio. The Young's moduli of random polycrystals in Ti-1553 and β-phase binary Ti alloys (Ti–Cr [42], Ti–V [43–45], and Ti–Nb [46–48]) calculated via the VRH approximation are also compared.

lowest Young's modulus of the XY-scan product, 58.5 ± 1.2 GPa in the Y (SD)-axis (E_2 for XY-scan in Table 1), is lower than the E_{RP} value by more than 20 GPa and close to that of the single crystal in the <100> direction. This indicates that Young's modulus of LPBF products can be considerably lowered via texture control.

The elastic constants of β-Ti alloys are believed to vary with the electron-atom ratio (e/a) [42]. Therefore, Young's moduli of various β-Ti alloys are compared based on the e/a ratio, where the e/a ratios for the random polycrystal of Ti-1553 alloy and XY-scan products were 4.10 and 4.14, respectively [8]. Fig. 7b shows a comparison between the Young's modulus in the Y-axis of the XY-scan product (E_2 for XY-scan in Table 1), which is the lowest Young's modulus among the XY- and X-scan products, and the Young's modulus of the random polycrystal E_{RP} of alloy Ti-1553 with respect to the e/a ratio. The E_{RP} values of various β-phase binary Ti alloys (Ti–Cr [42], Ti–V[43–45], and Ti–Nb [46–48]), which were calculated using Eq. (3), are presented for comparison. The Young's modulus of random polycrystalline E_{RP} in binary Ti alloys decreases with decreasing e/a ratio. Alloy Ti-1553 has a low e/a ratio, which means that its β-phase stability is quite low. Owing to the low e/a ratio, the E_{RP} value of Ti-1553 was relatively low compared to that of binary Ti alloys. The Young's modulus along the Y-axis of the XY-scan product (E_2 for the XY-scan in Table 1) was lower than all the E_{RP} values of the binary Ti alloys, even though the E_{RP} value of XY-scan product was comparable to those of the binary Ti alloys. This further supports the validity of texture control.

4. Discussion

4.1. Concept and calculation procedure of inverse self-consistent approximation for the elastic stiffness of a single crystal constituting LPBF-processed Ti-1553 alloy products

The Ti-1553 products obtained in this study exhibited both crystallographic and morphological textures (anisotropic grain shapes), leading to orthorhombic elastic symmetry with nine independent elastic stiffness components. The elastic stiffness components of a single crystal were extracted from those of polycrystals using an inverse self-consistent (iSC) approximation [36]. The SC approximation, which was originally presented independently by Hershey [34] and Kröner[35], is a well-known method for distinguishing the elastic stiffness components of polycrystals from those of a single crystal. The iSC approximation facilitates an "inverse" analysis for calculating the elastic stiffness components of a single crystal from those of the polycrystal.

This section describes the calculation procedure for the iSC approximation after a brief explanation of the SC approximation. Our previous study [36] provided a calculation procedure for the SC approximation method based on Eshelby's ellipsoidal inclusion theory [37] and the effective medium approximation [38]. Notably, the SC approximation can consider the elastic interaction between constituent grains by combining Eshelby's inclusion theory and the effective medium approximation. The effective elastic stiffness matrix (6 × 6) of a polycrystal ($\mathbf{c}^{\mathrm{pc}}$) is expressed as

$$\mathbf{c}^{\mathrm{pc}} = \left\langle \mathbf{c}^{\mathrm{SC}(i)} \mathbf{A}^{(i)} \right\rangle \left\langle \mathbf{A}^{(i)} \right\rangle^{-1}, \tag{4}$$

where $\mathbf{c}^{\mathrm{SC}(i)}$ is the elastic stiffness matrix of the i-th single-crystal obtained by converting the coordinate system of the elastic stiffness of the single crystal using the Euler angles ψ_1, φ, and ψ_2. These conversions orient the north pole of the crystal parallel to the x_3-axis (Z(BD)). $\langle \mathbf{X} \rangle$ denotes the orientational average of matrix $\mathbf{X}$. In the present case, $\langle \mathbf{X} \rangle$ was calculated for all the EBSD data points, assuming that each data point corresponded to a single-crystal grain. The shape of the grain was considered by introducing a strain concentration factor $\mathbf{A}^{(i)}$, which is defined as follows:

$$\overline{\boldsymbol{\varepsilon}}^{\mathrm{SC}(i)} = \mathbf{A}^{(i)} \overline{\boldsymbol{\varepsilon}}^{\mathrm{pc}(i)}, \tag{5}$$

where $\overline{\boldsymbol{\varepsilon}}^{\mathrm{pc}(i)}$ is the average strain in the polycrystal and $\overline{\boldsymbol{\varepsilon}}^{\mathrm{SC}(i)}$ is the average strain in the i-th single-crystal. The matrix form of the strain concentration tensor $\mathbf{A}^{(i)}$ evaluates the elastic strain in a single crystal, which depends on the grain shape and the difference in the elastic stiffness between the single crystal and the polycrystalline matrix. Matrix $\mathbf{A}^{(i)}$ is calculated according to Eshelby's equivalent inclusion theory [37] as follows:

$$\mathbf{A}^{(i)} = \left[\mathbf{I} + \mathbf{S}^{(i)} \left(\mathbf{c}^{\mathrm{pc}} \right)^{-1} \left(\mathbf{c}^{\mathrm{SC}(i)} - \mathbf{c}^{\mathrm{pc}} \right) \right]^{-1}, \tag{6}$$

where $\mathbf{I}$ is an identity matrix and $\mathbf{S}^{(i)}$ is the matrix notation of the Eshelby tensor. $\mathbf{S}^{(i)}$ depends on the elastic stiffness of the polycrystalline matrix and shape of the single crystal. The calculation of $\mathbf{S}^{(i)}$ is provided in the literature [49,50] and described in Appendix B of our previous study [36]. To calculate $\mathbf{S}^{(i)}$, the grain shape was regarded as a triaxial ellipsoid whose surface was defined as follows:

$$\frac{x_1'^2}{a_1^2} + \frac{x_2'^2}{a_2^2} + \frac{x_3'^2}{a_3^2} = 1, \tag{7}$$

where the coordinate axes x_1', x_2', and x_3' are aligned along the x_1, x_2, and x_3 axes of the reference coordinate system, respectively (Fig. 8a). In Eshelby's inclusion theory, grains are approximated as triaxial ellipsoids because the stress and strain fields within a triaxial ellipsoid become uniform, allowing the evaluation of stress and strain states. Therefore, grain shape was approximated as a triaxial ellipsoid. By calculating $\mathbf{S}^{(i)}$ and the crystallographic texture, the SC approximation evaluates both the grain shape and the crystallographic orientation of each grain. In the SC calculation, $\mathbf{c}^{\mathrm{pc}}$ that satisfies Eqs. (4) and (6) was calculated.

By contrast, in the iSC approximation, the elastic stiffness components of a single crystal, $\mathbf{c}^{\mathrm{SC}}$, were optimized using multiple regression analysis to minimize the difference between the effective ($\mathbf{c}^{\mathrm{pc}}$) and measured (c_{ij}^{meas}) elastic stiffnesses of a polycrystal, which is defined by the root mean square (rms):

$$\mathrm{rms} = \sqrt{\frac{\sum_{i,j}^{i=3,j=3} \left(\frac{c_{ij}^{\mathrm{pc}} - c_{ij}^{\mathrm{meas}}}{c_{ij}^{\mathrm{meas}}} \right)^2}{9}}. \tag{8}$$

The optimization of $\mathbf{c}^{\mathrm{SC}}$ was achieved using the Nelder–Mead simplex algorithm [51]. Notably, to determine $\mathbf{c}^{\mathrm{SC}}$ using the iSC approximation, the number of independent components of $\mathbf{c}^{\mathrm{pc}}$ must be the same as or larger than that of $\mathbf{c}^{\mathrm{SC}}$. In this study, the former was nine as measured using RUS-LDI, and the latter was three for a cubic single crystal.

When the iSC approximation was applied to the Ti-1553 alloy products, the aspect ratios of the ellipsoidal grains along the x_3' axis, a_3/a_2, were set as 3.2 and 7.4 for the XY- and X-scan products, respectively, based on the EBSD grain boundary maps shown in Fig. 4. The aspect ratios of the ellipsoidal grains along the x_1' axis, a_1/a_2, were set to 2.4 for both cases.

4.2. Elastic stiffness components of a single crystal constituting Ti-1553 alloy products prepared by LPBF

Table 2 lists the elastic stiffness components c_{ij} of a Ti-1553 single crystal constituting the LPBF-processed Ti-1553 alloy products, calculated using the iSC approximation. The averaged c_{ij} components and standard deviations for c_{ij} of a single crystal constituting the LPBF-processed Ti-1553 products (iSC) were obtained from eight samples, including the XY- and X-scan products. The c_{ij} values of a Ti-1553 single crystal prepared using the floating zone (FZ) method and measured using RUS combined with electromagnetic acoustic resonance (EMAR) [31] are shown for comparison. As shown in Table 2, the elastic stiffness components of a single crystal constituting the LPBF-processed Ti-1553 products evaluated using iSC were almost the same as those of a single

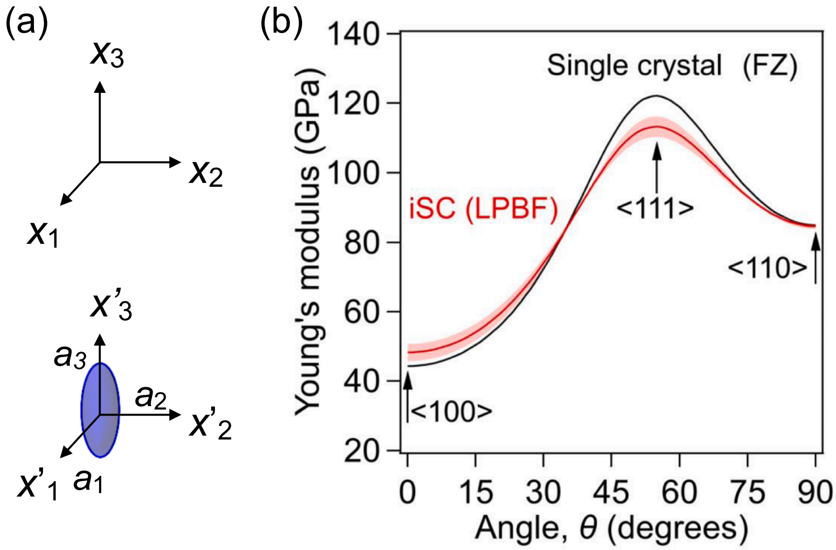

Fig. 8. (a) Schematic of the grain shape in the XY- and X-scan products, approximated as a triaxial ellipsoid. (b) Directional dependence of Young's modulus of a Ti-1553 single crystal constituting the LPBF-processed Ti-1553 products, as evaluated using the elastic-stiffness components c_{ij} obtained through iSC approximation. Directional dependence of Young's modulus for a Ti-1553 single crystal [31] prepared by the FZ method is provided for comparison.

Table 2
Elastic stiffness components c_{ij} (GPa) of a Ti-1553 single crystal constituting the LPBF-processed Ti-1553 products, calculated using the iSC approximation, and those of a Ti-1553 single crystal prepared by the FZ method [31]. The averaged c_{ij} components and standard deviations were obtained from eight samples including XY- and X-scan products.

	c_{11}	c_{12}	c_{44}
iSC (LPBF)	140.3 ± 3.5	106.5 ± 2.9	42.3 ± 1.3
FZ	135.1	104.2	46.2

crystal prepared using the FZ method.

Fig. 8b shows the directional dependence of Young's modulus of a single crystal constituting the LPBF-processed Ti-1553 products, obtained using iSC, and that of a single crystal prepared by the FZ method as a function of angle θ. The angle θ (0–90°) is defined as an angle from <100> through <111> to <110> of a cubic crystal. The lines and shadows in the iSC calculations represent the average and standard deviation, respectively, calculated from eight samples. The directional dependence of Young's modulus is almost the same between a single crystal constituting the LPBF-processed Ti-1553 products (iSC) and a single crystal prepared by the FZ method, even though Young's modulus is slightly different in the <111> and <100> directions.

The EDS analyses indicated that there was almost no elemental segregation in the LPBF-processed Ti-1553 alloy, suggesting that elemental segregation hardly affects the elastic properties of the alloy. This observation is consistent with the fact that a single crystal constituting the LPBF-processed Ti-1553 alloy exhibited nearly the same elastic stiffness as a single crystal prepared by the FZ method, which has a homogeneous elemental distribution.

To discuss the small differences in the elastic properties between a single crystal constituting the LPBF-processed Ti-1553 products (iSC) and the crystal prepared by the FZ method, their elastic constants are compared on the basis of electron-atom ratio (e/a), because the elastic constants of β-Ti alloys are believed to vary with the e/a ratio which is determined by the chemical composition [42].

Fig. 9 shows (a) the shear modulus c' for the $\{110\}<1\bar{1}0>$ shear, (b) bulk modulus B, (c) Young's modulus in the <100> direction (E_{100}), and (d) anisotropy factor A ($= c_{44}/c'$) in a single crystal constituting the LPBF-processed Ti-1553 products (iSC) and the single crystal prepared by the FZ method, as a function of e/a ratio. In the iSC approximation, the average value and standard deviation were obtained from eight samples. For comparison, the elastic constants for binary β-Ti alloy single crystals (Ti-Cr [42], Ti-V [43–45], and Ti-Nb [46–48]) are also presented. As evident from Fig. 9a, the shear modulus c' strongly depends on the e/a ratio. Similarly, the B, E_{100}, and A values are dominated by the e/a ratio (Fig. 9b–d). The e/a ratio of the Ti-1553 single crystal prepared by the FZ method was 4.10, and this low e/a ratio, indicating low β-phase stability, results in a low c' value (Fig. 9a). In the single crystal prepared by the FZ method, this low c' value leads to a high anisotropy factor A and low Young's modulus E_{100} because A and E_{100} are the function of c': $A = c_{44}/c'$ and $E_{100} = 9 / (1/B + 3/c')$ [31]. However, in a single crystal constituting the LPBF-processed Ti-1553 products (iSC), the c' and E_{100} values are slightly higher than those of a single crystal prepared by the FZ method. The anisotropy factor A in a single crystal constituting the Ti-1553 products (iSC) is slightly lower than that of a single crystal prepared by the FZ method. These differences could be attributed to the compositional differences between the LPBF products and the single crystals prepared via the FZ method, as gas atomization during the LPBF processes increases the concentration of Mo due to the evaporation of Ti and Al, which slightly increases the e/a ratio to 4.14 [8].

Here, ω-phase formation is examined based on the elastic properties which are sensitive to ω-phase formation. Since the elastic properties in a single crystal constituting the LPBF-processed Ti-1553 products are well-consistent with those of a single crystal prepared by the FZ method except for the small difference caused by composition changes during LPBF, it is deduced that ω-phase formation was successfully suppressed in the XY- and X-scan products prepared by the LPBF process, which is consistent with the electron diffraction patterns in Fig. 5. These results indicate that the single β-phase state is retained in the LPBF-processed Ti-1553 alloy products, even though stability of the bcc structure in a Ti-1553 alloy is quite low.

The formation of high-density dislocations also affects the elastic modulus [52,53]. During the LPBF process, thermal strain caused by elemental segregation generates dislocations in LPBF-processed alloys [54]. In the LPBF-processed Ti-1553 alloy, elemental segregation hardly occurred; therefore, the dislocation density is estimated to be low, even though it was not directly evaluated in the present study. Thus, it is speculated that the effect of dislocations formed during the LPBF process on the elastic properties is minimal in the LPBF-processed Ti-1553 alloy. To validate this speculation, the effect of dislocation density on the

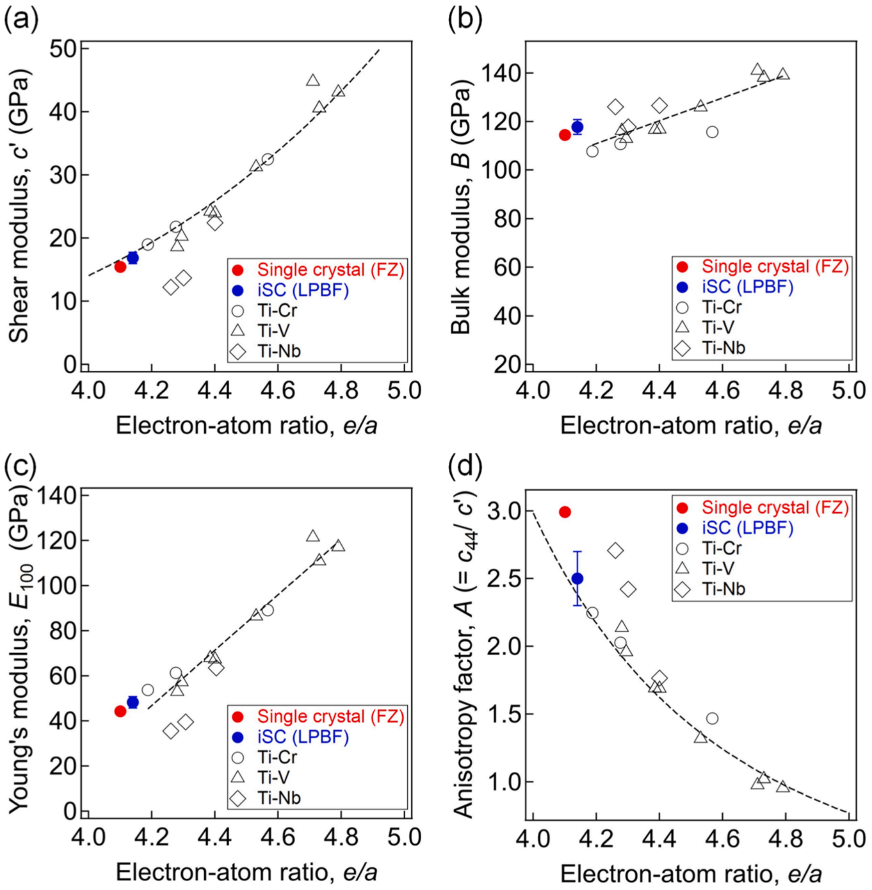

Fig. 9. Elastic constants of single crystal constituting the LPBF-processed Ti-1553 alloy products, calculated using the iSC approximation, as a function of electron-atom ratio (e/a): (a) shear modulus c'; (b) bulk modulus B; (c) Young's modulus in the <100> direction E_{100}; and (d) anisotropy factor A. Elastic constants for a Ti-1553 single crystal prepared by the FZ method [31] and binary β-Ti alloy single crystals (Ti–Cr [42], Ti–V [43–45], and Ti–Nb [46–48]) are shown for comparison.

elastic properties should be clarified by analyzing the dislocation density in LPBF-processed Ti-1553 alloy in future work.

4.3. Effective-mean-field theory for the elastic stiffness of a Ti-1553 single crystal containing ω phase

The one-dimensional intensity profiles of electron diffraction patterns (Fig. 5) indicated that a small fraction of the ω phase was formed. In metastable β-phase Ti alloys with low β-phase stability, the formation of the ω phase occurs in locally unstable β-phase regions, which are created by quenched-in statistical compositional fluctuations that inevitably exist, even when constituent elements are randomly distributed [14]. This suggests that the formation of the ω phase cannot be completely suppressed. Furthermore, in the Ti-1553 alloys prepared by the EBPBF process, a small amount of ω phase forms due to the preheating process for each building layer [21]. These facts highlight the importance of analyzing the effect of ω-phase formation on the elastic properties. Therefore, the potential effects of ω-phase formation on Young's modulus of a Ti-1553 alloy single crystal were examined by effective-mean-field (EMF) theory. EMF theory is based on Eshelby's inclusion theory [37], Mori-Tanaka's mean field theory [55] and the effective-medium approximation [38], and it yields reasonable elastic properties for a two-phase material even when the elastic stiffness of the inclusions is significantly different from that of the matrix phase [56]. The construction of EMF theory is detailed elsewhere [56] and its application to Ti-1553 alloy is described below.

By using the EMF method, the effective elastic stiffness $\overline{\mathbf{C}}_{(n+1)}$ of a Ti-1553 alloy that consists of a β-phase matrix and ω-phase inclusions with a volume fraction $f_\omega = (n+1)\Delta f$ is calculated through sequential calculations from $n = 0$ to $N-1$ as follows:

$$\overline{\mathbf{C}}_{(n+1)} = \left[\left(1-\frac{\Delta f}{1-n\Delta f}\right)\overline{\mathbf{C}}_{(n)} + \frac{\Delta f}{1-n\Delta f}\langle \mathbf{C}_\mathrm{I}\mathbf{A}_{(n)}\rangle\right]\times\left[\left(1-\frac{\Delta f}{1-n\Delta f}\right)\mathbf{I}+\frac{\Delta f}{1-n\Delta f}\langle \mathbf{A}_{(n)}\rangle\right], \tag{9}$$

where the boldface capital notation indicates a 6 × 6 matrix. $\overline{\mathbf{C}}_0$ and $\mathbf{C}_\mathrm{I}$ are the elastic stiffness matrix of the β-phase Ti-1553 alloy single crystal and ω-phase inclusion, respectively. $\langle\mathbf{X}\rangle$ is the orientational average of matrix $\mathbf{X}$. In the present case of $\beta+\omega$ phase, $\langle\mathbf{X}\rangle$ corresponds to the average of four ω-phase variants whose (0001) and $<11\overline{2}0>$ are aligned with the <111> direction and $<1\overline{1}0>$ of the β-phase matrix, respectively. Δf is defined as $1/N$, where N is the number of sequential calculations for f_ω to reach 100 %. In this study, $N = 100$ was sufficient to achieve the convergence of $\overline{\mathbf{C}}_{(n+1)}$. $\mathbf{I}$ is an identity matrix and $\mathbf{A}_{(n)}$ is expressed as follows:

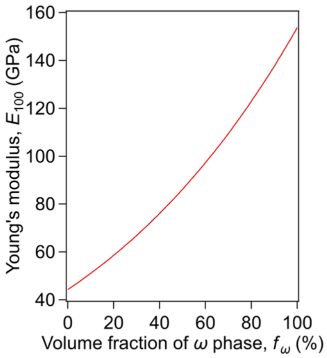

Fig. 10. The EMF calculations for Young's modulus in the <100> direction of a Ti-1553 alloy single crystal, E_{100}, as a function of the volume fraction of the ω-phase f_ω. The Ti-1553 alloy single crystal consists of a β-phase matrix and ω-phase inclusions.

$$\mathbf{A}_{(n)} = \left[\mathbf{S}_{(n)}\overline{\mathbf{C}}_{(n)}^{-1}\left(\mathbf{C}_{\mathrm{I}} - \overline{\mathbf{C}}_{(n)}\right) + \mathbf{I}\right]^{-1}, \tag{10}$$

where $\mathbf{S}_{(n)}$ is the matrix notation of the Eshelby tensor. As described in Section 4.1, $\mathbf{S}_{(n)}$ was calculated using $\overline{\mathbf{C}}_{(n)}$ and the shape of the inclusion.

Fig. 10 shows the calculated Young's modulus in the <100> direction of the Ti-1553 alloy single crystal, E_{100}, as a function of f_ω varying between 0 % and 100 %. In this calculation, the elastic stiffness of a Ti-1553 alloy single crystal, measured using the RUS-EMAR method [31] was used as the elastic stiffness of the β-phase matrix $\overline{\mathbf{C}}_0$. For the elastic stiffness of the ω-phase inclusion $\mathbf{C}_\mathrm{I}$, the values for the ω-phase single crystal in pure Ti [15] were used, as the elastic stiffness of the ω-phase in Ti-1553 has not been measured. The shape of the ω phase was assumed to be spherical. As shown in Fig. 10, Young's modulus E_{100} increases significantly with increasing f_ω. This indicates that the formation of the ω phase drastically increases the Young's modulus in the <100> direction.

4.4. Effects of ω-phase formation on the Young's modulus of XY- and X-scan products prepared by LPBF

The effect of ω-phase formation on the elastic properties of XY- and X-scan products prepared by LPBF was examined using the SC approximation. In the SC calculations, the elastic stiffness of a Ti-1553 single crystal with ω-phase inclusions calculated by the EMF theory was used. The aspect ratio a_3/a_2 of the grains was set to be 3.2 in the XY-scan products and 7.4 in the X-scan products, respectively, based on the EBSD grain boundary maps obtained from the YZ plane (Fig. 4), and the aspect ratios of the grains a_1/a_2 were set to 2.4 for both cases.

Fig. 11a shows the SC calculations for Young's modulus E_2 of the XY-scan products as a function of f_ω, where E_2 is the lowest Young's modulus obtained by the XY-scan. The averaged Young's modulus and standard deviations were obtained from four samples for each type of scan. The Young's modulus E_2 of the XY-scan products, measured by RUS-LDI, is also shown for comparison and this experimental value is independent of f_ω. The calculated Young's modulus E_2, SC(β+ω), increases significantly with increasing f_ω. Similarly, the calculated Young's modulus E_1 of the X-scan products, SC(β+ω), drastically increases with an increase in f_ω (Fig. 11b). A small f_ω, which is typically observed in β-Ti alloys prepared by AM (caused by the accumulation of heat in large-sized building [17,57]), could increase the Young's modulus relative to the values measured by RUS-LDI. The increment in Young's modulus could potentially be enhanced for β-Ti alloys with a lower β-phase stability such as Ti-1553, if the metastable β-phase is not successively retained. In other words, the suppression of ω-phase formation is important to decrease Young's modulus in β-Ti alloys prepared by LPBF, which is achieved by the rapid quenching rate of approximately 10^6 K/s in LPBF.

5. Conclusions

In β (body-centered cubic)-phase Ti–15Mo–5Zr–3Al (Ti-1553) alloys, the effects of anisotropic texture and microstructure formed by the laser powder bed fusion (LPBF)-type additive manufacturing (AM) process on their anisotropic elastic properties were investigated. Measuring all nine independent elastic stiffness components of the Ti-1553 products prepared by bidirectional scanning with (XY-scan) and without (X-scan) an interlayer rotation of 90° in LPBF revealed their strong elastic anisotropy and low Young's modulus, reaching below 60 GPa in the <100>-oriented direction of XY-scan products. Micromechanics calculations based on Eshelby's inclusion theory revealed that the single crystal constituting the Ti-1553 alloy products prepared by LPBF had almost the same elastic stiffness as that of a single crystal prepared by the floating zone method, indicating that the metastable β phase was successfully retained by suppressing ω-phase formation. The potential effects of ω-phase formation on the elastic properties of the LPBF-processed XY- and X-scan products were examined by effective-mean-field theory, which indicated that to decrease the Young's modulus in β-Ti alloys, both the

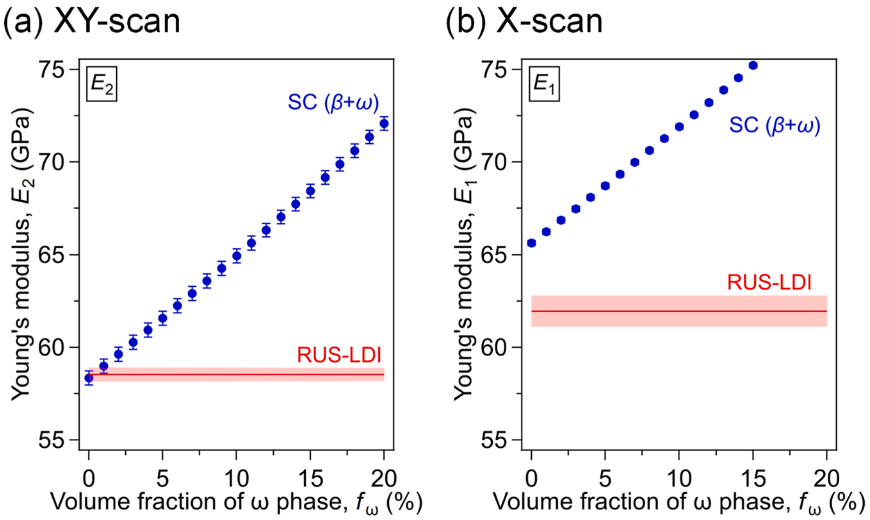

Fig. 11. The SC calculations for Young's modulus of Ti-1553 alloy products prepared by LPBF as a function of f_ω: (a) the Young's modulus E_2 of XY-scan products and (b) E_1 of X-scan products. The Young's moduli E_2 of the XY-scan products and E_1 of the X-scan products, measured by RUS-LDI, are also shown for comparison, and these experimental values are independent of f_ω.

texture control by scan strategy and the retention of metastable β phase by the rapid quenching in the LPBF process were important.

CRediT authorship contribution statement

Shota Higashino: Writing – original draft, Software, Investigation. **Daisuke Miyashita:** Software, Investigation. **Takuya Ishimoto:** Validation, Data curation. **Eisuke Miyoshi:** Software, Investigation. **Takayoshi Nakano:** Resources, Funding acquisition, Conceptualization. **Masakazu Tane:** Writing – review & editing, Supervision, Software, Resources, Funding acquisition, Conceptualization.

Declaration of Competing Interest

The authors declare that they have no known competing financial interests or personal relationships that could have appeared to influence the work reported in this paper.

Acknowledgments

This work was supported by the Core Research for Evolutionary Science and Technology (CREST) project of the Japan Science and Technology Agency (JST): CREST-Nanomechanics: Elucidation of macroscale mechanical properties based on understanding nanoscale dynamics for innovative mechanical materials [T.N., Grant No. JPMJCR2194]; the Japan Society for the Promotion of Science (JSPS) Grant-in-Aid for Transformative Research Areas [M.T., Grant Nos. 22H05291 and 24H01005]; the JSPS Grant-in-Aid for Scientific Research (B) [M.T., Grant No. 24K01201]; and the JSPS Grant-in-Aid for Challenging Research (Exploratory) [M.T., Grant No. 22K18890].

Appendix A. Supporting information

Supplementary data associated with this article can be found in the online version at doi:10.1016/j.addma.2025.104720.

Data availability

Data will be made available on request.

References

[1] R. Huiskes, H. Weinans, B. Van Rietbergen, The relationship between stress shielding and bone resorption around total hip stems and the effects of flexible materials, Clin. Orthop. Relat. Res. 274 (1992) 124–134, https://doi.org/10.1097/00003086-199201000-00014.

[2] M. Long, H.J. Rack, Titanium alloys in total joint replacement—a materials science perspective, Biomaterials 19 (1998) 1621–1639, https://doi.org/10.1016/S0142-9612(97)00146-4.

[3] A. Schuh, J. Bigoney, W. Hönle, G. Zeiler, U. Holzwarth, R. Forst, Second generation (low modulus) titanium alloys in total hip arthroplasty, Materwiss. Werksttech. 38 (2007) 1003–1007, https://doi.org/10.1002/mawe.200700230.

[4] P.C. Collins, D.A. Brice, P. Samimi, I. Ghamarian, H.L. Fraser, Microstructural control of additively manufactured metallic materials, Annu. Rev. Mater. Res. 46 (2016) 63–91, https://doi.org/10.1146/annurev-matsci-070115-031816.

[5] J.J. Lewandowski, M. Seifi, Metal additive manufacturing: A review of mechanical properties, Annu. Rev. Mater. Res. 46 (2016) 151–186, https://doi.org/10.1146/annurev-matsci-070115-032024.

[6] A. Basak, S. Das, Epitaxy and microstructure evolution in metal additive manufacturing, Annu. Rev. Mater. Res. 46 (2016) 125–149, https://doi.org/10.1146/annurev-matsci-070115-031728.

[7] O. Gokcekaya, T. Ishimoto, Y. Nishikawa, Y.S. Kim, A. Matsugaki, R. Ozasa, M. Weinmann, C. Schnitter, M. Stenzel, H.S. Kim, Y. Miyabayashi, T. Nakano, Novel single crystalline-like non-equiatomic TiZrHfNbTaMo bio-high entropy alloy (BioHEA) developed by laser powder bed fusion, Mater. Res. Lett. 11 (2023) 274–280, https://doi.org/10.1080/21663831.2022.2147406.

[8] T. Ishimoto, K. Hagihara, K. Hisamoto, S.-H. Sun, T. Nakano, Crystallographic texture control of beta-type Ti–15Mo–5Zr–3Al alloy by selective laser melting for the development of novel implants with a biocompatible low Young's modulus, Scr. Mater. 132 (2017) 34–38, https://doi.org/10.1016/j.scriptamat.2016.12.038.

[9] S.K. Sikka, Y.K. Vohra, R. Chidambaram, Omega phase in materials, Prog. Mater. Sci. 27 (1982) 245–310, https://doi.org/10.1016/0079-6425(82)90002-0.

[10] J.C. Williams, B.S. Hickman, D.H. Leslie, The effect of ternary additions on the decomposition of metastable beta-phase titanium alloys, Metall. Trans. 2 (1971) 477–484, https://doi.org/10.1007/BF02663337.

[11] B.S. Hickman, The formation of omega phase in titanium and zirconium alloys: A review, J. Mater. Sci. 4 (1969) 554–563, https://doi.org/10.1007/BF00550217.

[12] I. Ramsteiner, Omega-like diffuse X-ray scattering in Ti–V caused by static lattice distortions, Acta Mater. 56 (2008) 1298–1305, https://doi.org/10.1016/j.actamat.2007.11.015.

[13] J. Dutta, G. Ananthakrishna, S. Banerjee, On the athermal nature of the β to ω transformation, Acta Mater. 60 (2012) 556–564, https://doi.org/10.1016/j.actamat.2011.10.005.

M. Tane, H. Nishiyama, A. Umeda, N.L. Okamoto, K. Inoue, M. Luckabauer, Y. Nagai, T. Sekino, T. Nakano, T. Ichitsubo, Diffusionless isothermal omega transformation in titanium alloys driven by quenched-in compositional fluctuations, Phys. Rev. Mat. 3 (2019) 043604, https://doi.org/10.1103/PhysRevMaterials.3.043604.

[15] M. Tane, Y. Okuda, Y. Todaka, H. Ogi, A. Nagakubo, Elastic properties of single-crystalline ω phase in titanium, Acta Mater. 61 (2013) 7543–7554, https://doi.org/10.1016/j.actamat.2013.08.036.

[16] R. Duan, S. Li, B. Cai, W. Zhu, F. Ren, M.M. Attallah, A high strength and low modulus metastable β Ti-12Mo-6Zr-2Fe alloy fabricated by laser powder bed fusion in-situ alloying, Addit. Manuf. 37 (2021) 101708, https://doi.org/10.1016/j.addma.2020.101708.

[17] Y. Liu, L. Xu, C. Qiu, Development of an additively manufactured metastable beta titanium alloy with a fully equiaxed grain structure and ultrahigh yield strength, Addit. Manuf. 60 (2022) 103208, https://doi.org/10.1016/j.addma.2022.103208.

[18] X. Chen, C. Qiu, Development of a novel metastable beta titanium alloy with ultrahigh yield strength and good ductility based on laser power bed fusion, Addit. Manuf. 49 (2022) 102501, https://doi.org/10.1016/j.addma.2021.102501.

[19] S. Huang, P. Kumar, W.Y. Yeong, R.L. Narayan, U. Ramamurty, Fracture behavior of laser powder bed fusion fabricated Ti41Nb via in-situ alloying, Acta Mater. 225 (2022) 117593, https://doi.org/10.1016/j.actamat.2021.117593.

[20] J. Zhang, M.J. Bermingham, J. Otte, Y. Liu, Z. Hou, N. Yang, Y. Yin, M. Bayat, W. Lin, X. Huang, D.H. StJohn, M.S. Dargusch, Ultrauniform, strong, and ductile 3D-printed titanium alloy through bifunctional alloy design, Science 383 (2024) 639–645, https://doi.org/10.1126/science.adj0141.

[21] S.H. Sun, K. Hagihara, T. Ishimoto, R. Suganuma, Y.F. Xue, T. Nakano, Comparison of microstructure, crystallographic texture, and mechanical properties in Ti–15Mo–5Zr–3Al alloys fabricated via electron and laser beam powder bed fusion technologies, Addit. Manuf. 47 (2021), https://doi.org/10.1016/j.addma.2021.102329.

[22] A. Takase, T. Ishimoto, R. Suganuma, T. Nakano, Surface residual stress and phase stability in unstable β-type Ti–15Mo–5Zr–3Al alloy manufactured by laser and electron beam powder bed fusion technologies, Addit. Manuf. 47 (2021) 102257, https://doi.org/10.1016/j.addma.2021.102257.

[23] I. Ohno, Free vibration of a rectangular parallelepiped crystal and its application to determination of elastic constants of orthorhombic crystals, J. Phys. Earth 24 (1976) 355–379, https://doi.org/10.4294/jpe1952.24.355.

[24] H. Ogi, K. Sato, T. Asada, M. Hirao, Complete mode identification for resonance ultrasound spectroscopy, J. Acoust. Soc. Am. 112 (2002) 2553–2557, https://doi.org/10.1121/1.1512700.

[25] D. Healy, N.E. Timms, M.A. Pearce, The variation and visualisation of elastic anisotropy in rock-forming minerals, Solid Earth 11 (2020) 259–286, https://doi.org/10.5194/se-11-259-2020.

[26] T. Ishimoto, N. Morita, R. Ozasa, A. Matsugaki, O. Gokcekaya, S. Higashino, M. Tane, T. Mayama, K. Cho, H.Y. Yasuda, M. Okugawa, Y. Koizumi, M. Yoshiya, D. Egusa, T. Sasaki, E. Abe, H. Kimizuka, N. Ikeo, T. Nakano, Superimpositional design of crystallographic textures and macroscopic shapes via metal additive manufacturing—Game-change in component design, Acta Mater. 286 (2025) 120709, https://doi.org/10.1016/j.actamat.2025.120709.

[27] X. Luo, T. Song, A. Gebert, K. Neufeld, I. Kaban, H. Ma, W. Cai, H. Lu, D. Li, N. Li, Y. Li, C. Yang, Programming crystallographic orientation in additive-manufactured beta-type titanium alloy, Adv. Sci. 10 (2023) 2302884, https://doi.org/10.1002/advs.202302884.

[28] T. Ishimoto, K. Hagihara, K. Hisamoto, T. Nakano, Stability of crystallographic texture in laser powder bed fusion: Understanding the competition of crystal growth using a single crystalline seed, Addit. Manuf. 43 (2021) 102004, https://doi.org/10.1016/j.addma.2021.102004.

[29] K.P. Mingard, B. Roebuck, E.G. Bennett, M.G. Gee, H. Nordenstrom, G. Sweetman, P. Chan, Comparison of EBSD and conventional methods of grain size measurement of hardmetals, Int. J. Refract. Met. Hard Mater. 27 (2009) 213–223, https://doi.org/10.1016/j.ijrmhm.2008.06.009.

[30] N.L. Okamoto, S. Kasatani, M. Luckabauer, R. Enzinger, S. Tsutsui, M. Tane, T. Ichitsubo, Evolution of microstructure and variations in mechanical properties accompanied with diffusionless isothermal ω transformation in β-titanium alloys, Phys. Rev. Mater. 4 (2020) 123603, https://doi.org/10.1103/PhysRevMaterials.4.123603.

[31] S.-H. Lee, M. Todai, M. Tane, K. Hagihara, H. Nakajima, T. Nakano, Biocompatible low Young's modulus achieved by strong crystallographic elastic anisotropy in Ti–15Mo–5Zr–3Al alloy single crystal, J. Mech. Behav. Biomed. Mater. 14 (2012) 48–54, https://doi.org/10.1016/j.jmbbm.2012.05.005.

[32] X. Luo, D.D. Li, C. Yang, A. Gebert, H.Z. Lu, T. Song, H.W. Ma, L.M. Kang, Y. Long, Y.Y. Li, Circumventing the strength–ductility trade-off of β-type titanium alloys by defect engineering during laser powder bed fusion, Addit. Manuf. 51 (2022) 102640, https://doi.org/10.1016/j.addma.2022.102640.

[33] A. Takase, T. Ishimoto, R. Suganuma, T. Nakano, Lattice distortion in selective laser melting (SLM)-manufactured unstable β-type Ti-15Mo-5Zr-3Al alloy analyzed

by high-precision X-ray diffractometry, Scr. Mater. 201 (2021) 113953, https://doi.org/10.1016/j.scriptamat.2021.113953.

[34] A.V. Hershey, The elasticity of an isotropic aggregate of anisotropic cubic crystals, J. Appl. Mech. 21 (1954) 236–240, https://doi.org/10.1115/1.4010899.

[35] E. Kröner, Berechnung der elastischen Konstanten des Vielkristalls aus den Konstanten des Einkristalls, Z. Phys. 151 (1958) 504–518, https://doi.org/10.1007/BF01337948.

[36] M. Tane, K. Yamori, T. Sekino, T. Mayama, Impact of grain shape on the micromechanics-based extraction of single-crystalline elastic constants from polycrystalline samples with crystallographic texture, Acta Mater. 122 (2017) 236–251, https://doi.org/10.1016/j.actamat.2016.09.040.

[37] J. Douglas Eshelby, The determination of the elastic field of an ellipsoidal inclusion, and related problems, Proc. R. Soc. Lond. A Math. Phys. Sci. 241 (1957) 376–396, https://doi.org/10.1098/rspa.1957.0133.

[38] D.A.G. Bruggeman, Berechnung verschiedener physikalischer Konstanten von heterogenen Substanzen. I. Dielektrizitätskonstanten und Leitfähigkeiten der Mischkörper aus isotropen Substanzen, Ann. Phys. 416 (1935) 636–664, https://doi.org/10.1002/andp.19354160705.

[39] M. Tane, S. Akita, T. Nakano, K. Hagihara, Y. Umakoshi, M. Niinomi, H. Nakajima, Peculiar elastic behavior of Ti–Nb–Ta–Zr single crystals, Acta Mater. 56 (2008) 2856–2863, https://doi.org/10.1016/j.actamat.2008.02.017.

[40] R. Hill, The elastic behaviour of a crystalline aggregate, Proc. Phys. Soc. A 65 (1952) 349–354, https://doi.org/10.1088/0370-1298/65/5/307.

[41] D. Mainprice, R. Hielscher, H. Schaeben, Calculating anisotropic physical properties from texture data using the MTEX open-source package, Geol. Soc., Lond., Spec. Publ. 360 (2011) 175–192, https://doi.org/10.1144/SP360.10.

[42] E.S. Fisher, D. Dever, Relation of the c' elastic modulus to stability of b.c.c. transition metals, Acta Met 18 (1970) 265–269, https://doi.org/10.1016/0001-6160(70)90033-7.

[43] L.A. Ahlberg, O. Buck, N.E. Paton, Effects of hydrogen on anisotropic elastic properties of bcc Ti-alloys, Scr. Met 12 (1978) 1051–1054, https://doi.org/10.1016/0036-9748(78)90023-6.

[44] E.S. Fisher, A Review of Solute Effects on the Elastic Moduli of BCC Transition Metals. in: Physics of Solid Solution Strengthening, Springer New York, Boston, MA, 1975, pp. 199–225, https://doi.org/10.1007/978-1-4684-0757-0_8.

[45] K.W. Katahara, M.H. Manghnani, E.S. Fisher, Pressure derivatives of the elastic moduli of BCC Ti-V-Cr, Nb-Mo and Ta-W alloys, J. Phys. F: Met. Phys. 9 (1979) 773–790, https://doi.org/10.1088/0305-4608/9/5/006.

[46] R. Hermann, H. Hermann, M. Calin, B. Büchner, J. Eckert, Elastic constants of single crystalline β-Ti70Nb30, Scr. Mater. 66 (2012) 198–201, https://doi.org/10.1016/j.scriptamat.2011.10.039.

[47] H.W. Jeong, Y.S. Yoo, Y.T. Lee, J.K. Park, Elastic softening behavior of Ti–Nb single crystal near martensitic transformation temperature, J. Appl. Phys. 108 (2010) 063515, https://doi.org/10.1063/1.3486212.

[48] C.N. Reid, J.L. Routbort, R.A. Maynard, Elastic constants of Ti–40 at% Nb at 298 °K, J. Appl. Phys. 44 (1973) 1398–1399, https://doi.org/10.1063/1.1662365.

[49] T. Mura, Micromechanics of defects in solids, 2nd, revised edition ed., Springer Netherlands, Dordrecht, 1987. ⟨https://doi.org/10.1007/978-94-009-3489-4⟩.

[50] N. Kinoshita, T. Mura, Elastic fields of inclusions in anisotropic media, Phys. Status Solidi A 5 (1971) 759–768, https://doi.org/10.1002/pssa.2210050332.

[51] J.A. Nelder, R. Mead, A simplex method for function minimization, Comput. J. 7 (1965) 308–313, https://doi.org/10.1093/comjnl/7.4.308.

[52] H.M. Ledbetter, S.A. Kim, Low temperature elastic constants of deformed polycrystalline copper, Mater. Sci. Eng. A 101 (1988) 87–92, https://doi.org/10.1016/0921-5093(88)90053-6.

[53] J.A. Benito, J. Jorba, J.M. Manero, A. Roca, Change of Young's modulus of cold-deformed pure iron in a tensile test, Metall. Mater. Trans. A 36 (2005) 3317–3324, https://doi.org/10.1007/s11661-005-0006-6.

[54] M. Li, R. Ma, Y. Ren, S. Chang, L. Li, New insights on dislocation forming mechanism of nickel-based superalloy fabricated by laser powder bed fusion, J. Mater. Res. Tech. 30 (2024) 4303–4309, https://doi.org/10.1016/j.jmrt.2024.04.105.

[55] T. Mori, K. Tanaka, Average stress in matrix and average elastic energy of materials with misfitting inclusions, Acta Met. 21 (1973) 571–574, https://doi.org/10.1016/0001-6160(73)90064-3.

[56] M. Tane, T. Ichitsubo, Effective-mean-field approach for macroscopic elastic constants of composites, Appl. Phys. Lett. 85 (2004) 197–199, https://doi.org/10.1063/1.1769587.

[57] C. Qiu, Q. Liu, Multi-scale microstructural development and mechanical properties of a selectively laser melted beta titanium alloy, Addit. Manuf. 30 (2019) 100893, https://doi.org/10.1016/j.addma.2019.100893.